Fig S1. Characterization and quantification of RWD behavior. Related to Fig 1.

a. Video frames (front view) showing hand locations in a representative trial at different time points during the reach.

b. Schematic of the measurement of hand rotation direction (black vector) and finger pointing direction (orange vector) as represented by key points on left digits. The hand supinates to a horizontal position with the lift, advance and to a palm up position for licking.

c. Quantification of waterspout aiming score ($\cos(\delta)$) to measure the hand posture for aim location and posture toward waterspout.

d. Quantification of digit open/extend size for waterspout grasp, quantified as the length of the hand rotation vector.

e. Schematic for quantifying hand to mouth distance (d) and hand rotation vector (s) upon lick. The hand was maintained close to the mouth and supinated during tongue protrusions.

f. Schematic for quantifying the hand rotation score ($\cos(\theta)$) relative to the horizontal reference vector (y). Value 1 means the palm faces up and is fully supinated. -1 indicates the palm faces down and fully pronated. 0 means left hand is vertical and facing towards the right. Typically, the hand rotation score is close to -1 before lift, 0 at grasp and close to 1 at hand lick.

g. Top: hand posture progression at lift (the fingers slightly closed and flexed), at aim (palm rotated toward target), at advance endpoint (fingers extend and open for grasp) and at hand-lick (hand can be closed or open). Bottom: distribution of hand rotation angle as a reflection of palm-facing direction. Data from 6229 lifts, aims, advance endpoints; and 119584 licks from 70 sessions in 25 mice. Note the near 180-degree hand supination from reach-grasp (pronated) to withdraw-lick (supinated).

h. Spatial contour map of hand locations (side view) at lift, aim and advance endpoint. Contours indicate probability starting from $0.01/mm^2$ with equal increment of $0.01/mm^2$; 6229 trials from 70 sessions in 25 mice across five target locations; +, waterspout location.

i. Occurrence probability of sequential RWD movements relative to the reach endpoint. Results of 3924 trials from 70 sessions in 25 mice reaching for P2.

j. Hand and oral movement time series for waterspout positions P1, P3 and P5.

k. Mapping of the action phases with movement time series. Each dot is a movement time point in the latent space.

l–s. Behavior modulation by waterspout locations: latency to lift (**l**), reach duration (**m**), premature lick before waterspout contact (**n**), reach end position relative to waterspout (**o**), path length (**p**), distance from aim onset of reach to the target (**q**), change of digit aiming score during aim (**r**), probability of significant acceleration peaks during aim and advance (**s**). 70 sessions from 25 mice. Median ± interquartile range. Horizontal lines in boxplots indicate 75%, 50%, and 25% percentile. Whiskers represent data point span to 90% or 10% percentile. See Supplementary table for statistics.

Fig S2. Cortex-wide calcium activity during RWD. Related to Fig 2.

a. Registered atlas areas superimposed on an image of the dorsal cortex. MOB, main olfactory bulb; MOs, secondary motor cortex; MOp, primary motor cortex; RSP, retrosplenial cortex; SSp, primary somatosensory cortex; tr, trunk; ll, lower limb; ul/un, upper limb and unknown region; orf, orofacial; bfd, barrel field; VIS, visual cortex. White dots outline the cortex; yellow horizontal line shows olfactory bulb and neocortex boundary; yellow vertical line shows the midsagittal suture.ds.

b. Coronal brain sections showing the laminar pattern of PN types labeled by driver lines crossed to reporter mice. Bottom row is zoom-in, and rotated view of the dashed box annotated with layers L1-L6.

c. PN markers across cortical layers. Immunostaining of Cux1 (red) and Tle4 (blue), was carried out after mRNA in situ hybridization of *Fezf2* (magenta) in *PlxnD1;Ai148* (green) mice. Scale bar, 100 μm.

d. Temporal occurrence of RWD movements after training at location P2. Top, lift and first hand-lick probability (Prob.) distribution relative to waterspout contact. Bottom, average lick frequency aligned to waterspout contact. (n = 3924 trials from 70 sessions in 25 mice)

e. Average sequential activity frames at 200 ms intervals centered on waterspout contact (black box) during RWD from P2. (n = 9 sessions from 5 mice for PN^{Emx1}; 7 sessions from 4 mice for IT^{Cux1}; 11 sessions from 4 mice for IT^{PlxnD1}; 12 sessions from 6 mice for PT^{Fezf2}; 10 sessions from 5 mice for CT^{Tle4}.)

f. Average cortex-wide calcium activity at the five target locations during the whole RWD process. Note the increase of ipsilateral (left) hemisphere activity as the target moved from P1 to P5.

g. Summary and comparison of ROIs. Top: ROIs by thresholding of normalized GLM performance. Bottom, ROIs by thresholding of normalized activity.

h. Calcium activity change of ipsilateral ROIs.

i. Quantification of the performance of the GLM encoding model for different ROIs.

Fig S3. Photoinhibition survey across cortical nodes during RWD. Related to Fig 3.

a. ChR2-assisted closed-loop photoinhibition of cortical areas during RWD. Crosses ('x') represent the center of several previously characterized cortical areas, from anterior to posterior: anterior lateral motor cortex (ALM; Guo, 2014), rostral forelimb area (RFA; Tennant, 2011), rostral forelimb orofacial area (RFO; An, 2023), caudal forelimb area (CFA; Tennant, 2011), and primary motor cortex for the upper limb (Sauerbrei, 2020; Muñoz-Castañeda, 2022). Black squares indicate the centers of region of interest in this study. +, bregma; scale, 0.5 mm.

b. Cumulative distribution of supination latency relative to hand lift in closed-loop inhibition and control trials of each node in contralateral and ipsilateral hemisphere. *d*, two-sample Kolmogorov-Smirnov

distance. (n = 5 mice, see Supplementary table for statistics)

c. Changes in occurrence probability of constituent movements between inhibition and control trials for each contra- and ipsi-lateral cortical node. Performance of component movements, reach, withdraw, and drink were quantified with the probability of successful waterspout contact, full hand supination, and lick respectively. (n = 5 mice)

d. Closed-loop inhibition of contralateral MOs-c impaired action progression represented as an ethogram from an example session. Actions accomplishment is color coded. The relative onset and duration of the inhibition light for each trial are indicated with cyan shades. Note inhibition attenuates the completion of the RWD sequence.

e. Closed-loop MOs-c inhibition resulted in increased hand reversals during reach, decreased target contact after lift, supination after grasp, and hand lick after grasp. (n = 5 mice, two-sample KS test.)

f. Movement time series during closed-loop MOs-c inhibition. Exemplary hand movements in relation to the target, hand rotation, and lick from several consecutive control (gray) and inhibition (tortoise) trials are shown. Movement profiles are normalized. Note that upon termination of inhibition, animals immediately resumed and completed the action sequence of RWD.

Fig S4. MOs-c PN-type-specific contribution to RWD. Related to Fig 3.

a. Left, viral expression of the inhibitory opsin GtACR1 in MOs-c of an *Emx1-Cre* mouse. Scale, 1 mm. Right, impaired reach and withdraw upon closed-loop inhibition of MOs-c PNs. (n = 5 PN^{Emx1} mice.)

b. Decrease of lift probability to initiate reaching for contralateral targets upon prolonged MOs-c PN inhibition (n = 15 sessions from 8 PN^{Emx1} mice. Left, Wilcoxon rank sum test. Right, mixed-design ANOVA, inhibition $F_{1,56} = 10.74$, $p < 0.01$; inhibition × target $F_{4,56} = 4.46$, $p < 0.01$).

c. Decreased coordination between hand upward-downward movement and mouth open-close movement during drinking measured by their coherence (Mixed-design ANOVA, inhibition $F_{1,494} = 12.96$, $^{**}p < 0.01$).

d. Cortical, striatal, and thalamic projections from different MOs-c PN types. IT neurons show projection to the contralateral cortex and no projection to thalamus. Note the rare projection of IT^{Cux1} to striatum as compared with that of IT^{PlxnD1}. PT^{Fezf2} and CT^{Tle4} both project to thalamus. Scale, 1 mm.

e. Effect on reach, withdraw, and consumption upon prolonged IT inhibition (n = 8 sessions from 6 IT^{Cux1} mice and 12 sessions from 7 IT^{PlxnD1} mice. Reach: mixed-design ANOVA; IT^{Cux1} $F_{1,28} = 0.06$, $p = 0.81$; IT^{PlxnD1} $F_{1,44} = 1.2$, $p = 0.30$. Boxplots for supination probability after waterspout contact, premature lick and variance of hand position upon licks: Wilcoxon rank sum test. Plots for hand rotation upon licks: two-sample KS test)

Fig S5. Electrophysiological recording from MOs-c during RWD. Related to Fig 4.

a. Action phase encoding in simultaneously recorded individual and population neurons in MOs-c. Raster panels show spikes of individual neurons in relation to actions. Right most panel shows action phase embedding in the latent space of population neural activity revealed by supervised CEBRA model in an example session (n = 108 neurons). Each dot represents a time point (1/240 s). Superimposed colors indicate different action phases.

b. Neuronal activity at different cortical depths relative to hand lift (0) from an exemplar session.

c. Fraction of activated neurons that peaked at different action phases during RWD.

d. Increase of movement encoding as the neural depth increases. $R^2 = 0.157$, $p = 9.73\times10^{-44}$. Movement encoding of individual neurons was represented by the deviance explained by a Poisson-GLM. See Methods.

e. Increase of peak activity as neural depth increases. $p = 1.48\times10^{-20}$.

f. Correlation between exemplar actual movement time series (gray) and GLM-predicted traces (orange) using simultaneously recorded spiking activity from an exemplar recording session. Movement time series include forward, upward, lateral hand position, and hand position in relation to waterspout or mouth. Spikes were binned in 20 ms bins to predict time series using GLM.

g. Population MOs-c activity decodes forelimb movement times series. Note the higher correlation with forelimb movement kinematics (orange) in relation to waterspout or mouth (magenta), but lower correlation with movements of other body parts (blue). Gray boxplots indicate cross-validated performance of the null model as control. (n = 106 sessions)

h. MOs-c activity decodes target locations indicated with cross-validated decoding accuracy of Naïve Bayes classifiers. Unfilled box plots indicate performance of the shuffled model as control. (n = 106 sessions)

Fig S6. Optogenetic tagging and PN-type specific behavioral correlates. Related to Fig 4.

a. Light-evoked spiking activity of all tagged PNs. The vertical dashed line indicates light pulse (blue bar) onset. (n = 26 IT^{Cux1}, 16 IT^{PlxnD1}, 50 PT^{Fezf2}, and 40 CT^{Tle4} neurons)

b. Average light-evoked activity of all tagged neurons across different neuron types. The delayed modulation after immediate activity upon light pulses suggests a recurrent connection in PT^{Fezf2}. Horizontal dashed lines are 0 reference.

c. Boxplots of reliability, jitter, and latency of light-evoked spikes of different PN types.

d. Activity tuning by target location from example IT^{Cux1}, IT^{PlxnD1}, PT^{Fezf2}, and CT^{Tle4} neurons. Vertical dashed lines: advance endpoint.

e. Waterspout target modulation index of distinct PN types across different action phases.

f. Average population neural trajectories along the first two principal dimensions for IT^{Cux1} and IT^{PlxnD1}.

Fig S7. Anatomical connections of MOs-c CT^{Tle4}. Related to Fig 5.

a. Comparison of CT^{Tle4} neurons (yellow) and pons-projecting PT neurons (magenta) in MOs-c. Only 8/144 red neurons show green fluorescence. Arrows indicate PT neurons.

b. Coronal brain sections show MOs-c CT^{Tle4} neurons (green) project axons exclusively to thalamus without terminals in midbrain or pons, while pons-projecting PT neurons (red) branches in brainstem with few terminals in thalamus.

c. Left, schematic for mono-synaptic input mapping of MOs-c CT^{Tle4} neurons with rabies tracing (RV). D, Day. The right two panels indicate the EGFP-expressing (yellow) and RV-expressing (magenta) neurons in the MOs-c injection site. Tle4 starters are labeled by both colors (white). Cyan, Nissl stain.

d. Coronal brain sections show presynaptic partners of MOs-c CT^{Tle4} in orbital frontal cortex (ORBl), sensorimotor cortex (MOp, SSp, SSs), thalamus (VAL, VM, PF, AV) and midbrain (PPN).

e. Combined retrograde (from MOs-c) and anterograde (from thalamus) tracing (schematic) revealed the recurrent connections between MOs-c and VAL/VM. A mix of AAV with Flp recombinase (*AAV-retro-Flp*) and Cre recombinase dependent GFP (*AAV-DIO-EGFP*) is injected into the MOs-c of *Tle4-CreER* mice. Flp dependent mCherry (*AAV-fDIO-mCherry*) is injected into the thalamus to express in

$TPN^{MOs\text{-}c}$. MOs-projecting TPNs also send branches to MOp and SSp-ul.

Fig S8. MOs-c CT^{Tle4} modulates thalamic dynamics. Related to Fig 6.

a. Optogenetic tagging of postsynaptic neurons of MOs-c CT^{Tle4} in thalamus.

b. Left, light-evoked PETH (top) and raster (bottom) activity of a MOs-c CT^{Tle4} postsynaptic neuron in thalamus ($TPN^{Tle4\text{-}post}$). Right, light response of 92 identified $TPN^{Tle4\text{-}post}$ (blue) compared with 210 not significantly modulated (gray).

c. Light-evoked spiking reliability and latency of all thalamic neurons. The same set of neurons were used for the following panels. (n = 92 $TPN^{Tle4\text{-}post}$ and 210 control (gray circles))

d. Facilitation of evoked activity of $TPN^{Tle4\text{-}post}$ indicated by a three-fold increase of neural activity upon the 5th light pulse (2.17) compared with that of the 1st one (0.57) with 20 Hz stimulation.

e. Action phase encoding in simultaneously recorded individual and population neurons in VAL/VM. Raster panels show spikes of individual neurons in relation to actions. Right most panel shows action phase embedding in the latent space of population neural activity revealed by supervised CEBRA model on an example session (n = 213 neurons). Each dot represents a time point (1/240 s). Superimposed colors indicate different action phases.

f. Left, recording thalamic neurons with MOs-c CT^{Tle4} inhibition. Right, average inhibition effect on all thalamus neurons across RWD phases. (n = 814 neurons)

g. Thalamic neuron activity difference between optogenetic inhibition and control conditions. Left, spike raster of a Group I neuron during RWD. Inhibition light was delivered around the lift in random half of the trials. Trials are grouped by inhibition light (bottom) and sorted by the duration between hand lift (orange ticks) and the advance endpoint (pink ticks). Black ticks, first hand licks to consume water. Right, heatmap showing the difference. (n = 814 neurons)

Fig S9. Effects of MOs-c PT^{Thal} on thalamic dynamics. Related to Fig 6.

a. Two-virus strategy (schematic) to label thalamus-branching PT neurons (PT^{Thal}, magenta). *AAV-retro-fDIO-Cre* is injected into the VAL/VM of *Fezf2-Flp* mice. A mix of Cre dependent mCherry (AAV-DIO-mCherry) and Flp recombinase dependent GFP (*AAV-fDIO-EGFP*) is injected to the MOs-c. This strategy indicates ~40% (545/1334 neurons) of Fezf2 neurons branch in thalamus (n = 2 mice). Arrows indicate double-labeled neurons. Scale, 1 mm for the whole section and 200 μm for zoom-in view.

b. Coronal brain sections show MOs-c PT^{Thal} neurons (magenta) collaterals in the striatum (Stri.), STN, ZI, and other midbrain and brainstem nuclei besides VAL/VM. Scale, 1 mm.

c. Electrophysiological recording of thalamus neurons upon optogenetic inhibition of thalamus-branching PT (PT^{Thal}) in MOs-c. Left, expressing GtACR1 in MOs-c PT^{Thal} neurons with the two-virus strategy. Right, average effect of MOs-c PT^{Thal} on the spontaneous firing of 814 thalamic neurons. Neurons were divided into 92 decreased Group I, 439 non-modulated Group II, and 318 increased Group III.

d. Thalamic activity difference between MOs-c PT^{Thal} inhibition and control conditions. (n = 849 neurons)

SUPPLEMENTAL INFORMATION

Supplementary video 1

RWD behavior, 3D-reconstructed hand trajectories, and selected movement time series across different waterspout locations are shown. Movement components, including reach (lift, aim, advance), withdraw and drink, are superimposed on hand trajectory. Movement time series include hand to target distance, moving speed, rotation score and waterspout aiming score of the left reaching hand. Example trials from three waterspout locations were arranged sequentially. The movie is played at 1/40 of the original behavior speed.

Supplementary table 1

Detailed statistical information.

Figure S1

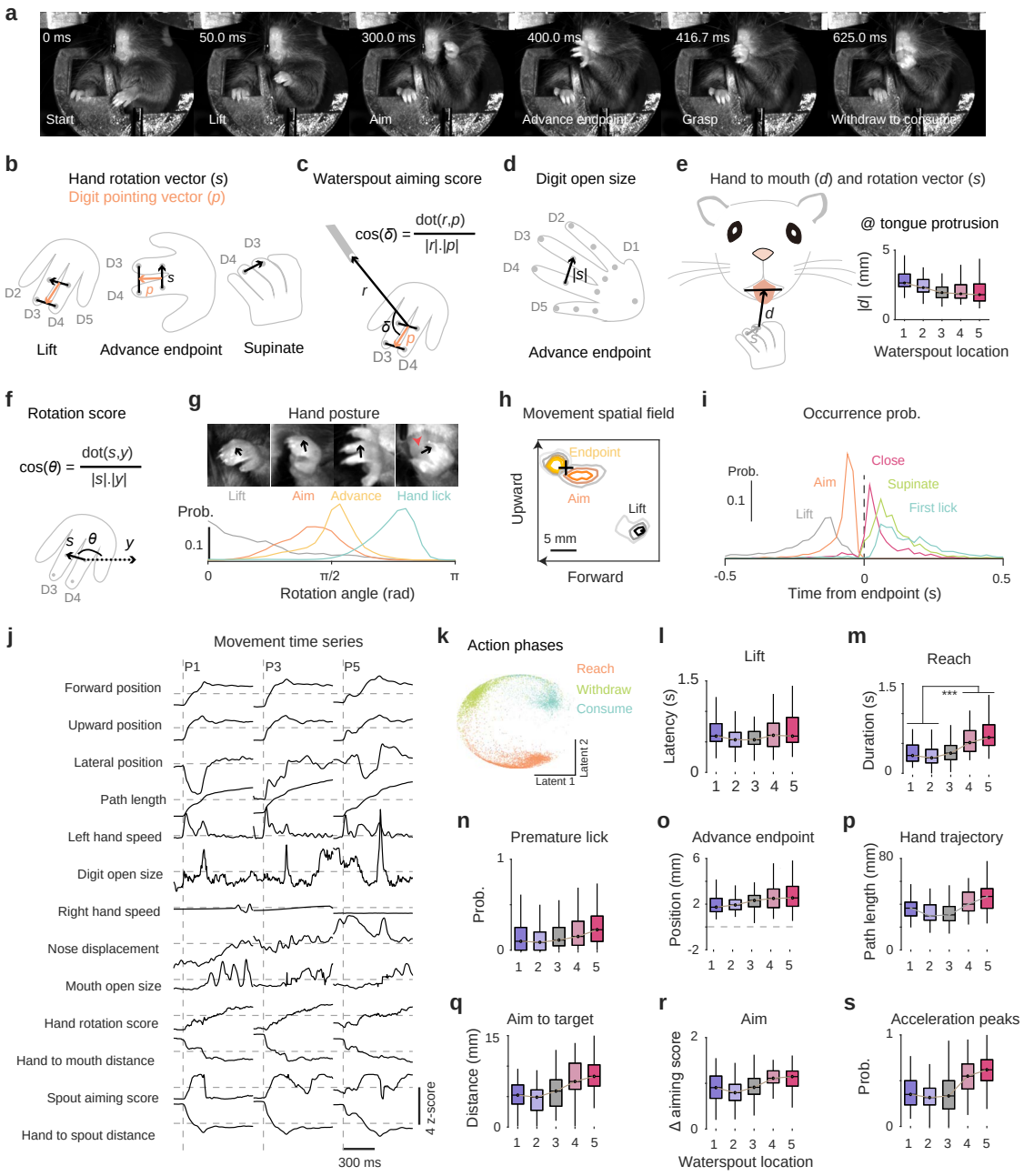

Figure S2

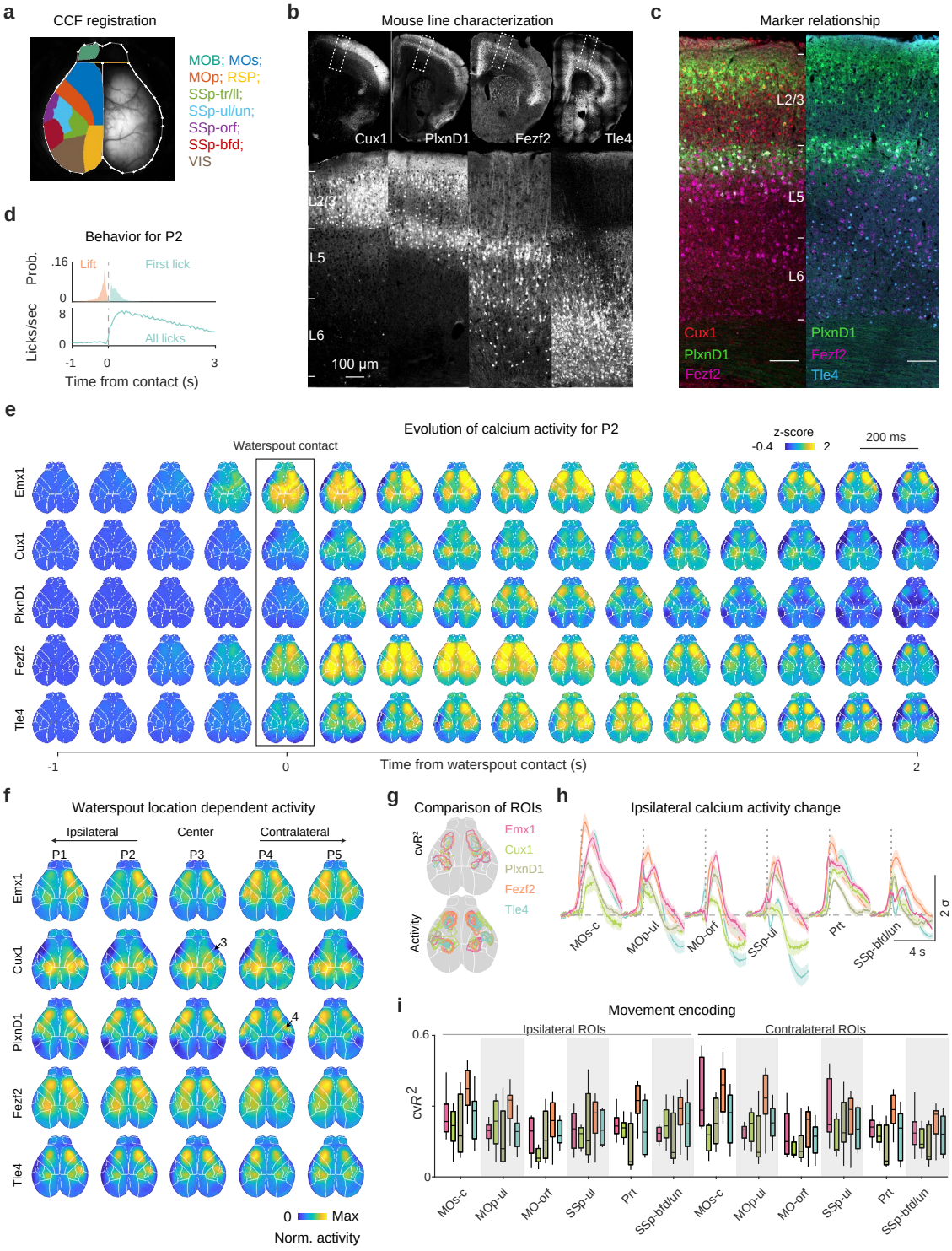

Figure S3

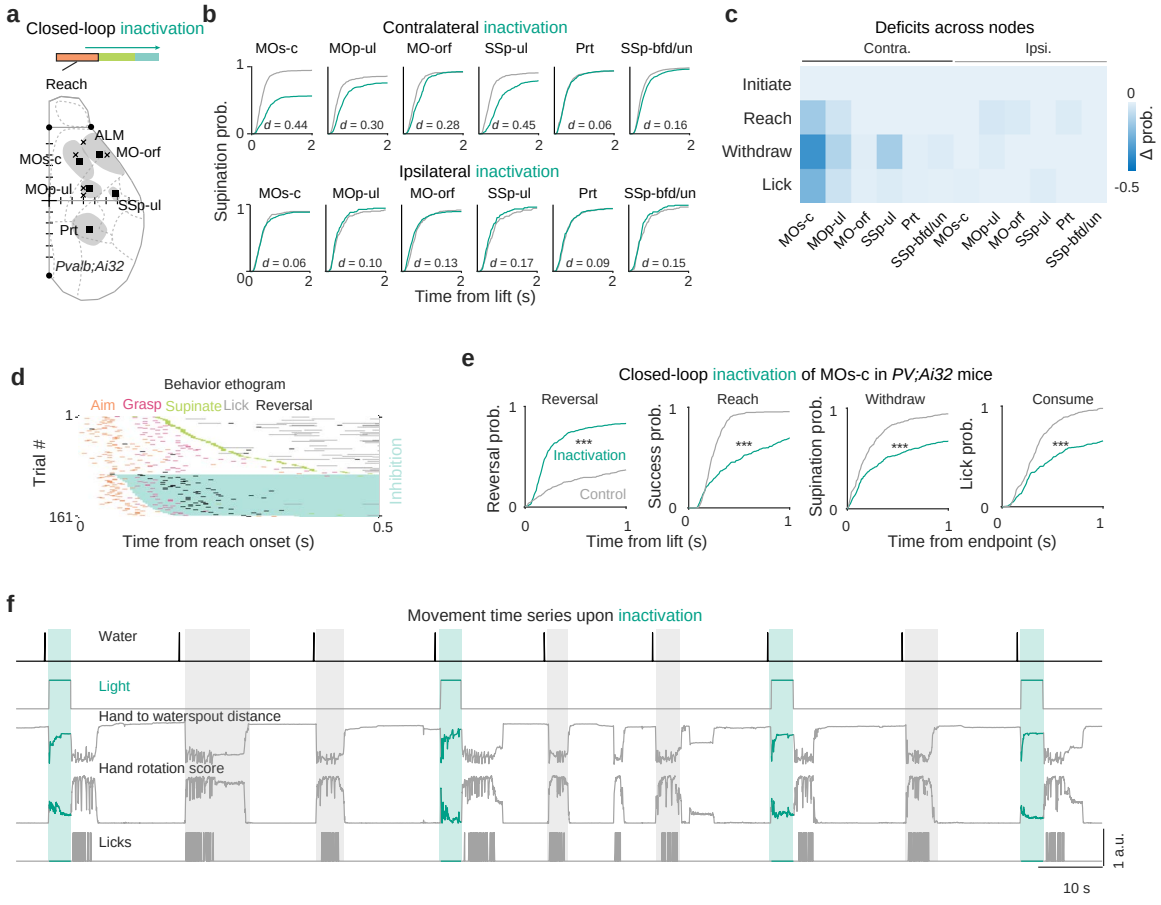

Figure S4

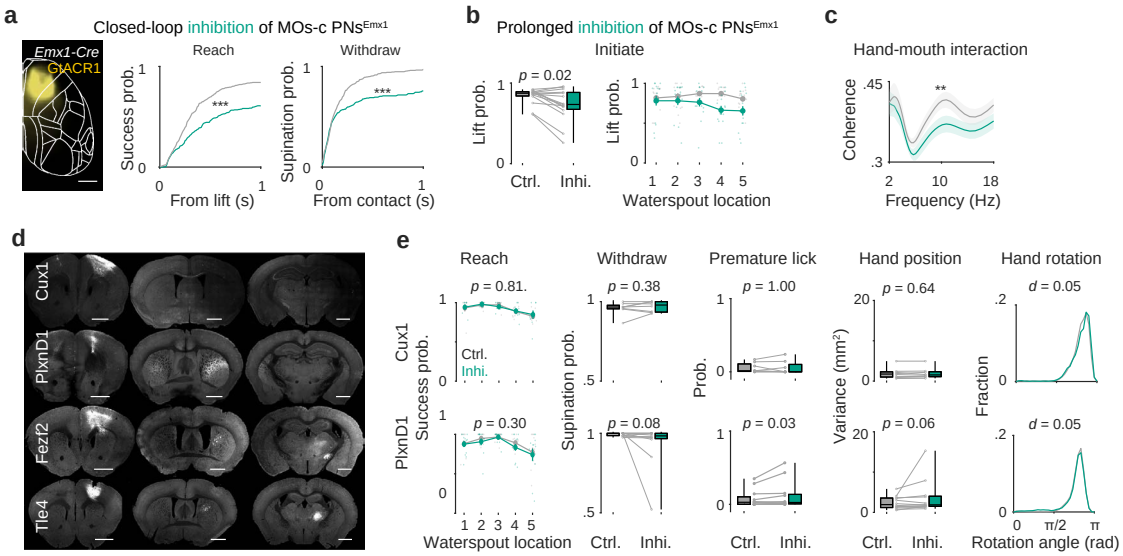

Figure S5

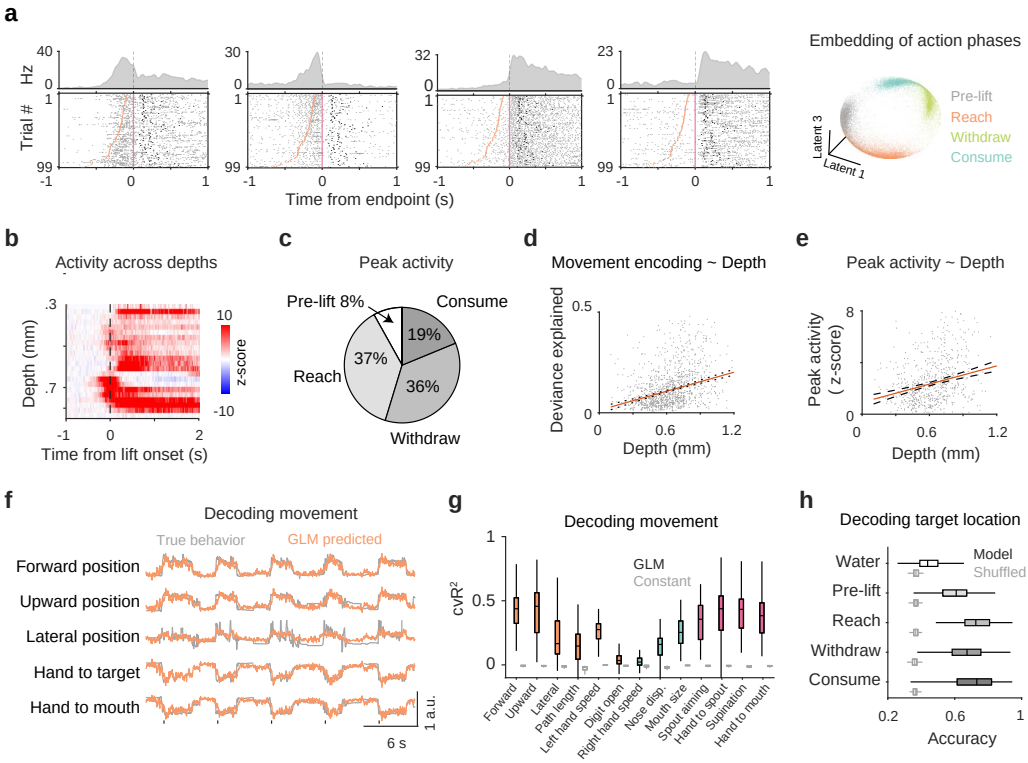

Figure S6

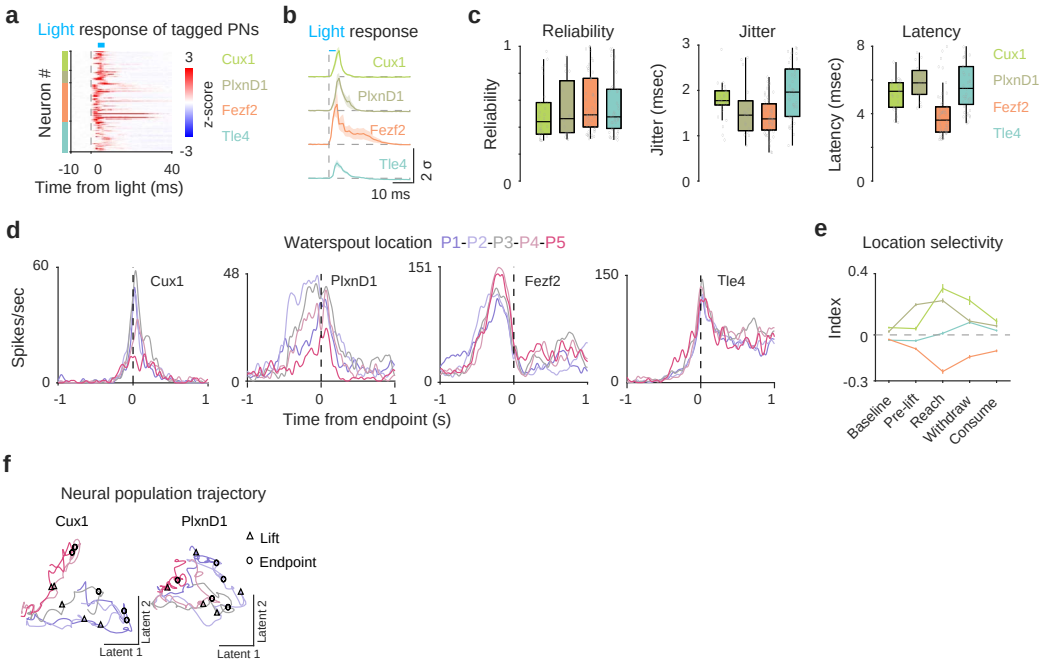

Figure S7

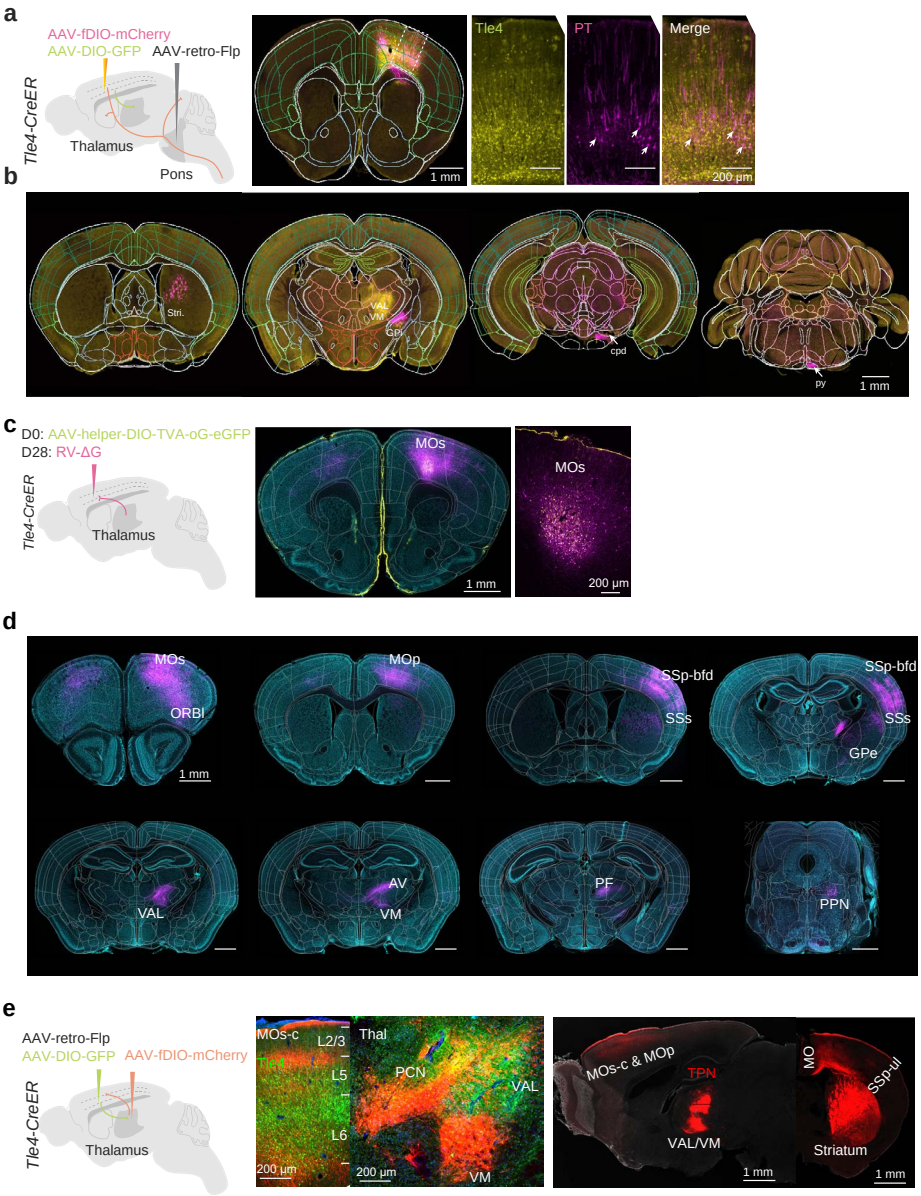

Figure S8

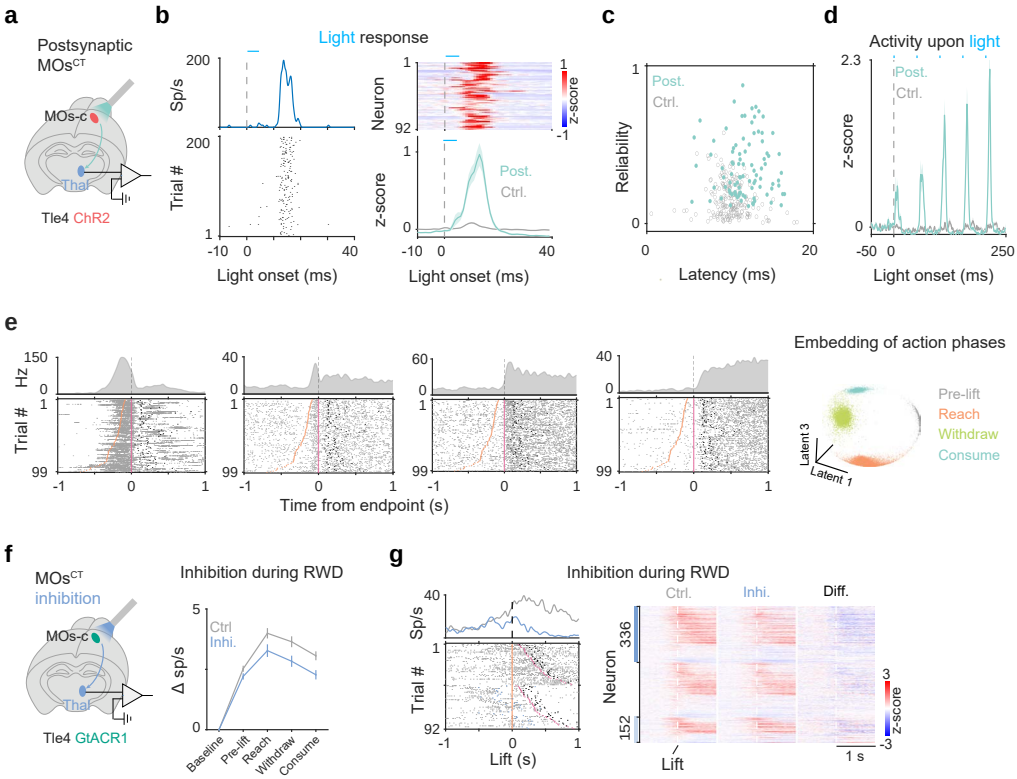

Figure S9